Classification of Cloud Phase Using Combined Ground-Based Polarization Lidar and Millimeter Cloud Radar Observations Over the Tibetan Plateau

Yuxuan Bian, Liping Liu, Jiafeng Zheng, Songhua Wu, and Guangyao Dai

***Abstract*— The distributions of cloud phases play an important role in influencing the weather and climate system. The characteristics of clouds above the Tibetan Plateau (TP) can profoundly affect regional and global atmospheric circulation. To research the distributions of cloud phases in the TP region, a retrieval algorithm was developed based on the combination of polarization lidar and millimeter cloud radar measurements and applied to the data from a comprehensive field campaign on the central TP in the summer of 2014. The structure and phase of four different types of clouds were retrieved accordingly, which validates the reliability of the algorithm. The result shows that the occurrence frequency of low clouds remains around 50%, which is very high throughout the whole day in Nagqu, Tibetan in summer. The liquid and mixed cloud frequencies are higher in the morning and afternoon, while ice cloud mainly occurs from the afternoon to midnight. Liquid and ice phase distributions show an inverse relationship in the atmospheric layer from 2 to 8 km in height. Meanwhile, the proportion of the liquid phase to the cloud top is significantly higher than that to the cloud body, which indicates that the supercooled water is more likely to appear at the cloud top than in the cloud. The fractional probabilities of the ice phase and liquid phase in the total cloud top phase intersect at about −26.7 °C.**

***Index Terms*— Atmospheric measurements, cloud phase classification, cloud radar, lidar.**

I. Introduction

CLOUDS are water droplets, supercooled liquid water, ice crystals, or a mixture of them condensed (deposited) from water vapors in the atmosphere [1]. Clouds in the atmosphere determine the surface precipitation and the balance of atmospheric radiation and play an important role in the climate system [2]. The Fifth Assessment Report of the Intergovernmental Panel on Climate Change states that aerosol-cloud interaction is the largest uncertainty factor in the research of the global radiation balance [3], [4]. To classify the clouds with the phase properties of cloud particles, there are liquid clouds composed of water droplets, ice clouds composed of ice crystals, and mixed-phase clouds composed of both supercooled water and ice crystals. Mixed-phase clouds dominate the distribution of global cloud covers [5]. In a mixed-phase cloud system, the complicated interactions and phase changes among water vapor, liquid droplets, and ice crystals inside the cloud make its structure particularly complex and difficult to be simulated accurately [6], [7]. Because of the lack of sufficient understanding of the fine phase distribution in the cloud, the Bergeron process in the mixed-phase cloud is also considered to be the most important source of error when the global climate model is used to simulate the phase distribution in the cloud [8].

The Tibetan Plateau (TP) is the tallest (average elevation of more than 4000 m above sea level) and largest (area of about 2.5×10^6 km^2) plateau in the world [9]. The high land surface supports the vigorous exchanges of heat and moisture with the middle troposphere, which profoundly influences the regional and global atmospheric circulation, especially the Asian monsoon, through its thermal and dynamic forcing [10]. Compared with those in other regions, the special atmospheric thermodynamics, circulation, and high topography can cause significant differences in the microphysical characteristics of clouds and precipitation [11]. The cloud and precipitation microphysical processes over the TP are different from those in low-altitude areas [12]. The occurrence frequency of cumulus convection in the TP is higher than that in the plain area, while the convective cloud top and strong echo top are both lower from the ground, and the horizontal scale of the convective system is also smaller [13].

For a long time, many studies have pointed out that the lack of observational data related to the microphysical properties of mixed-phase clouds is an important factor restricting the accuracy of model simulations [14]. The most direct way to detect the cloud phase is aircraft observation. Early aircraft observations found that in the temperature range of −40 °C to 0 °C, water in both liquid and ice phases coexisted. Moss and Johnson [15] developed an automatic technique that can differentiate between liquid water droplets and ice particles and calculate the ratio between ice and liquid phase based on data from the Particle Measuring System (PMS) probes carried on the aircraft. Because part of the ice phase particles appears spherical, this method of analyzing the phase state based on 2-D cloud particle probe images may lead to

Manuscript received 20 April 2023; revised 7 August 2023; accepted 6 September 2023. Date of publication 11 September 2023; date of current version 20 September 2023. This work was supported by the National Natural Science Foundation of China under Grant 41975043. *(Corresponding author: Liping Liu.)*

Yuxuan Bian and Liping Liu are with the State Key Laboratory of Severe Weather (LASW), Chinese Academy of Meteorological Sciences, Beijing 100081, China (e-mail: bianyx@pku.edu.cn; liulp@cma.gov.cn).

Jiafeng Zheng is with the Plateau Atmosphere and Environment Key Laboratory of Sichuan Province, School of Atmospheric Sciences, Chengdu University of Information Technology, Chengdu 610225, China (e-mail: zjf1988@cuit.edu.cn).

Songhua Wu and Guangyao Dai are with the Ocean Remote Sensing Institute, Ocean University of China, Qingdao 266100, China (e-mail: wush@ouc.edu.cn; dgy1105@163.com).

Digital Object Identifier 10.1109/TGRS.2023.3313798

errors of up to two or three times [16]. Aircraft observations can provide information on important microphysical features in clouds; however, due to their low spatial and temporal resolution and the difficulty of carrying out long-term continuous observations, high-resolution remote sensing detection methods are essential to analyze the vertical distribution and temporal evolution of particles in different phases in the cloud [17].

Weather radars (S, C, and X-band meteorological radars) mainly observe the 3-D structure of precipitation echoes but have limited ability to detect clouds, while remote sensing instruments with relatively short wavelengths, such as millimeter-wave cloud radar (MMCR) and lidar, are the main means of detecting clouds. In the early 1990s, the Microwave Remote Sensing Laboratory developed a dual-wavelength (35/94 GHz) cloud radar, which was mainly used to observe ice clouds, supercooled water, and raindrop spectra [18]. The dual wavelength ratio, which was not sensitive to droplets smaller than 500 μm diameters, was used to distinguish ice clouds from liquid clouds in this study. In the mid-1990s, the U.S. Department of Energy launched a long-term Atmospheric Radiation Measurement Program (ARM), and some unattended, vertically oriented Ka-band (35 GHz) cloud radars were placed in several regions where climate characteristics changed significantly. This radar can observe nonprecipitation clouds and weak precipitation clouds with reflectivity between -50 and 29 dBZ, and the data quality is reliable [19], [20]. It is used to analyze the macro and micro characteristics of clouds, radiation characteristics, and their relationship with climate change [21]. Shupe et al. [22] measured and retrieved the liquid and ice phases in mixed-phase clouds with the combination of this radar and another W-band cloud radar. Their study found that when both supercooled water and ice crystals were significantly present in mixed-phase clouds, the Doppler spectra of cloud radars showed a bimodal distribution, and the signals of these two peaks came from liquid phase and ice phase particles, respectively [22].

In recent years, lidar has gradually been widely used for remote sensing detection of atmospheric composition characteristics [23]. Compared with weather radar and cloud radar, the detection signal band used by lidar technology is way shorter; therefore, lidar has outstanding detection sensitivity on aerosols, water vapor, and other atmospheric components of smaller size, and also has good detection ability on cloud droplets [24], [25], [26]. The elastic scattering lidar can usually receive elastic backscattering signals in the 355/532/1064 nm band and derive the backscattering coefficient of cloud particles. Combined with the polarization detection technology, by separating the parallel polarization component and the perpendicular polarization component of the scattered signal, the depolarization ratio can be solved, to distinguish the scattering of spherical particles and nonspherical particles and distinguish the aerosols, cloud droplets, and ice crystals [27]. Noel et al. [28] retrieved the spatial distribution of ice phase particles with different forms in the cloud based on airborne polarization lidar measurements. Xie et al. [29] used a polarization lidar to observe in northwestern China. By combining the backscattering coefficient and depolarization ratio data for inversion, the ratio of the ice phase to the liquid phase in the cloud was calculated [29].

Combining the instrument principle and a series of observational research results, it can be found that MMCR and polarization lidar have their advantages in observing cloud microphysical properties, but they also have obvious defects. The signal of MMCR has a strong response to ice crystals, but it is relatively difficult to detect small droplets; lidar has a strong detection ability for droplets, but the signal attenuates too fast in the cloud, making it difficult to detect the interior characteristics of the entire cloud [30]. Because of the difference in wavelength between these two types of instruments, the scattering of cloud droplets to their signal should be described with different theories. The scattering of cloud droplets to cloud radar signal (millimeter-wave) should be categorized into Rayleigh scattering, which means the intensity of the scattering light is proportional to the sixth power of the particle size, while the intensity of the scattering light to lidar signal (visible to near-infrared) is proportional to the square of the particle size according to the Mie scattering theory [31]. This difference suggests that millimeter-wave cloud-measuring radar is more sensitive to particle size and has difficulty identifying cloud bases [32]. Meanwhile, Mie scattering of lidar signal results in stronger attenuation; therefore, the combination of cloud radar and lidar can make up for the respective deficiencies of the two instruments when observing mixed-phase clouds that contain both ice and liquid-phase hydrometeors. Wang and Sassen [33] built a parameterization scheme based on the extinction coefficient profiles from lidar and the echoes from cloud radar to retrieve ice water content and effective ice crystal size. Khanal and Wang [34] evaluated the errors of this parameterization by comparing the results with aircraft observations. Shupe et al. [35] identified cloud phases with MMCR and polarization lidar at an ARM site. Zhao et al. [36] systematically expounded the advantages and errors of various algorithms to retrieve cloud microphysical properties. It can be seen that the retrieval algorithm based on millimeter-wave radar and lidar is the most suitable for the retrieval of cloud phase states, especially for mixed-phase clouds [36]. By combining lidar measurements and cloud radar Doppler spectra data, Luke et al. [37] derived the distribution of the supercooled water into mixed-phase clouds.

Because of the relative lack of field observational experiments on the microphysical characteristics of clouds and precipitations on the TP, little is known about the cloud phase behavior there [38]; moreover, the specific natural environment on the TP results in unique cloud and precipitation properties, especially when compared to low-altitude regions [39], and can prominently limit the simulation capabilities of numerical weather prediction models. He et al. [40] and Zhao et al. [41] investigated the microphysical properties of clouds on the TP based on lidar and cloud radar observations, respectively. Because of the limitation of each instrument, it is, however, very difficult to effectively classify the cloud phases on the TP with only one of these remote sensing instruments [40], [41].

To develop the understanding of this field, a classification algorithm to classify the phase distribution of hydrometeors

in the cloud was established in this study, relying on the observations with polarization lidar and MMCR in the TP. The vertical and temporal distributions of cloud phase states in the TP in summer were investigated accordingly.

The remainder of this article is organized as follows. Section II introduces the experiment, instruments, and methodologies used in this study; Section III shows the details of the phase classification results for four different types of cloud, and also the statistical analysis of cloud phase classification results. Finally, a conclusion is drawn in Section IV.

II. Data and Methodology

A. Data and Instrumentation

The Third TP Atmospheric Scientific Experiment (TIPEX-III), which began formally in 2014, was initiated jointly by the China Meteorological Administration (CMA) and several other scientific institutes [10]. The main purpose of this experiment is to research the cloud microphysical characteristics of the TP.

Within the TIPEX-III framework, an intensive field campaign was conducted from July 8th to August 16th in 2014 at Nagqu Meteorological Bureau (31.48°N, 92.06°E; 4508m above the sea level) over the central TP. An elastic-backscatter lidar and a vertical pointing MMCR were deployed at the weather station during the campaign to detect the vertical structures and microphysical properties of clouds. The GTS1 radiosondes (Nanjing Bridge Machinery Company Ltd., China) were launched two times per day (00:00 and 12:00 UTC) at the station [42]. Chinese standard time (UTC +8) is used in this study as local time. The height used in this study represents the altitude above ground level.

Water vapor, cloud, and aerosol lidar (WACAL) is a mobile Raman and elastic scattering lidar used to detect and investigate water vapor, clouds, and related atmospheric components. The system development and joint debugging were completed in June 2013 by the Ocean University of China and the Chinese Academy of Meteorological Sciences. This lidar adopts a three-wavelength emission system, which can continuously detect the vertical profiles of water vapor in the troposphere (within a height of 0.2–5 km) and clouds (within a height of 0.2–15 km), and obtain the mixing ratio of water vapor, cloud depolarization ratio, cloud base height, atmospheric extinction coefficient, and atmospheric backscattering coefficient profile. This system is installed in a container, which is convenient to be carried on the vehicle-mounted mobile platform for movement and can observe under different environmental conditions stably and reliably.

The POWERLITE DLS 9030 laser, which is a high-power, narrow-linewidth triple-frequency Nd:YAG pulsed laser produced by Continuum Company in the United States, is used as the laser emission system of WACAL, which can simultaneously emit pulsed lasers with three wavelengths of 355, 532, and 1064 nm. The elastic scattering signals (including 355, 532, and 1064 nm) and Raman scattering signals (including 386.7 and 407.5 nm) are received by a telescope array system composed of four Newtonian telescopes. Detailed information about WACAL can be found in [43].

In 2013, the Chinese Academy of Meteorological Sciences and the 23rd Research Institute of 2nd Academy, China Aerospace Science and Industry Corporation developed a new Ka-band MMCR. The radar frequency is 33.44 GHz, while the sensitivity can reach below −30 dBZ at 5 km, the detective range of height is from the ground to 15.3 km altitude, the echo intensity detective range is from −45 to 30 dBZ, and the maximum detective windspeed can reach ±18.54 m/s. The spatial and temporal resolution of MMCR is 30 m and 3 s, respectively. The detective quantities of MMCR include raw Doppler radar spectra data and reflectivity factors, mean Doppler velocity, Doppler spectrum width, and signal-to-noise ratio. Detailed information about MMCR can be found in [44].

B. Cloud Phase Classification Algorithm for the Combined Measurement of WACAL and MMCR

Based on WACAL and MMCR, a joint retrieval algorithm for the classification of the cloud phases is established. Fig. 1 shows an example of this classification process. The vertical profile of attenuated backscattering coefficient β with three-wavelength can be derived from WACAL measurement [see Fig. 1(b)]. This parameter is related to both the amount and the size of particles. The profile of depolarization ratio δ, which can indicate how spherical the particle is, can be calculated from the ratio between scattering signals of two different polarization directions with 532 nm wavelength [see Fig. 1(c)]. These two parameters include backscattering information from both clouds and aerosols. To determine the cloud boundary with lidar measurements, an automated method combining a "differential zero-crossing algorithm" and a "threshold algorithm" was considered [45]. The zero crossings of the first derivative of the backscatter intensity and a range-dependent threshold are used to identify the cloud base and top heights. For a detailed cloud boundary identification method and related comparative study, please refer to Wu et al. [46]. The cloud boundary estimated with this method are shown by the gray solid line in Fig. 1(b) and (c).

The zero-order and second-order moments of Doppler radar spectra, which are the radar reflectivity factor Z_e and the Doppler spectrum width σ_v, respectively, can be obtained from MMCR measurement [see Fig. 1(e) and (g)]. In the previous related studies, the mean Doppler velocity, as the first-order moment of Doppler radar spectra, always be used to evaluate the particle size with the assumption that the vertical air velocity can be ignored. This assumption is well suited for regions like the Arctic because the lower atmosphere tends to have high stability, but it cannot be used in this study because there is significant convective activity over TP [20]; therefore, the vertical air velocities have been retrieved from MMCR Doppler radar spectra in this campaign [44]. The particle fall velocity V_p shown in Fig. 1(f) can be directly calculated by subtracting vertical air velocity from Doppler velocity. Here, negative velocities represent downward motion.

According to the different responses of products like δ, β, Z_e, V_p, and σ_v to particles with different sizes and phases, a cloud phase classification algorithm has been built. Since WACAL cannot pass through thick clouds, phase identification

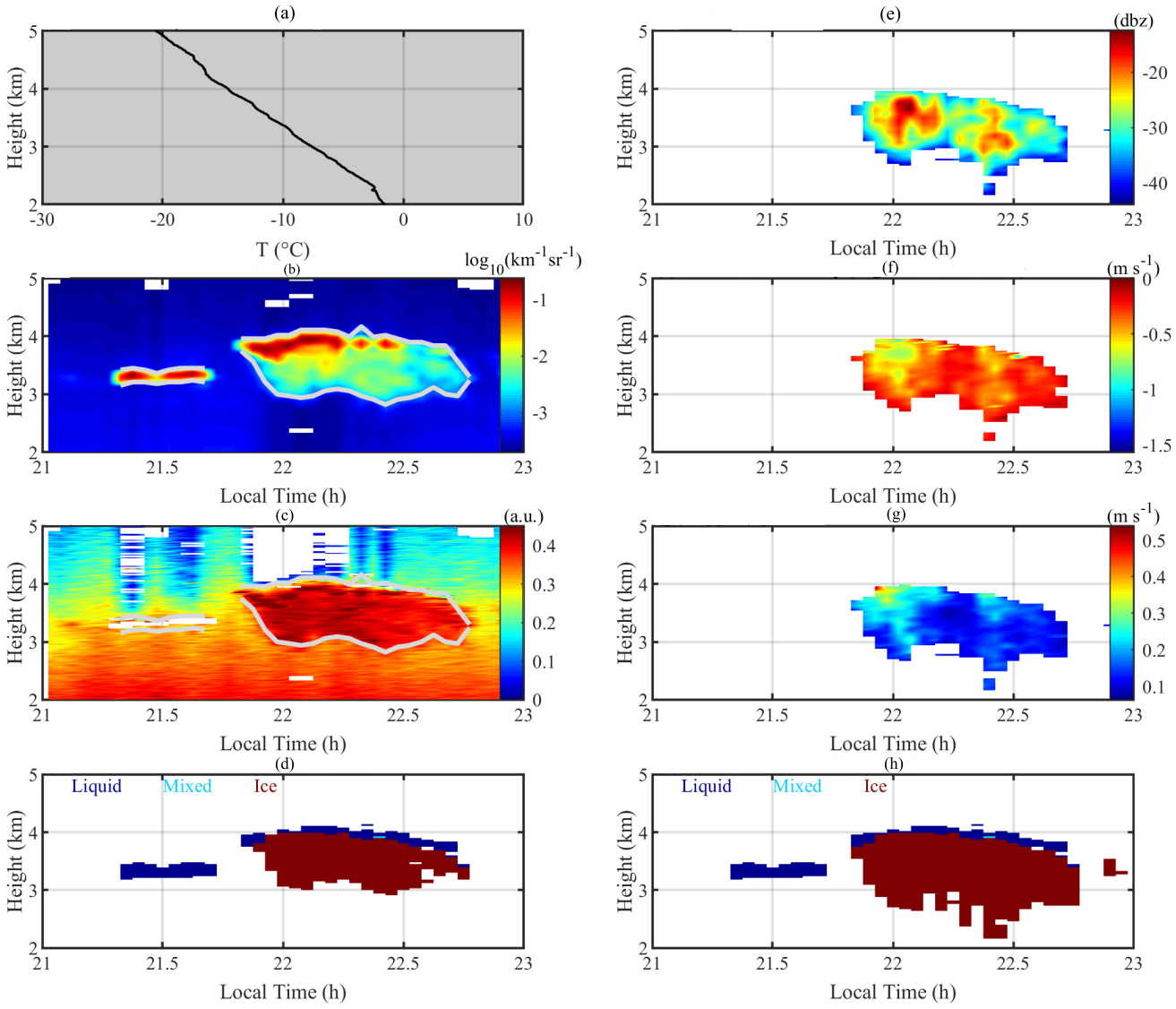

Fig. 1. Example of the cloud phase classification algorithm. (a) Radiosounding temperature profiles (shadow zone shows the zone with temperature between 0 °C and −40 °C). (b) 532 nm attenuated backscattering coefficients retrieved from WACAL measurement (gray line shows the estimated cloud boundary). (c) 532 nm lidar depolarization ratios retrieved from WACAL measurement (gray line shows the estimated cloud boundary). (d) Cloud phase distributions classified with WACAL and MMCR measurements in a lidar-detected zone (liquid phase: blue color; mixed phase: cyan color; and ice phase: brown color). (e) Radar reflectivity retrieved from MMCR measurement. (f) Particle fall velocities retrieved with MMCR measurements (positive velocities represent upward motion and negative velocities show downward motion). (g) Doppler spectrum widths retrieved with MMCR measurements. (h) Cloud phase distributions classified with WACAL and MMCR measurements in lidar-detected zone (liquid phase: blue color; mixed phase: cyan color; and ice phase: brown color), while both MMCR-detected and WACAL-detected regions are included.

is first performed in the area that lidar can detect. Nonspherical particles such as ice crystals have much higher δ than spherical particles like water droplets, while β of droplets are always higher due to the number concentration. By establishing reasonable thresholds of these parameters, the phase distribution of hydrometers at different heights in the cloud can be analyzed. Compared with applying fixed thresholds to attenuated backscattering coefficient and depolarization ratio separately, a better way is to separate liquid from ice phase with varying thresholds of β and δ. Following the discrimination method introduced by Hu et al. [47], the relationship between depolarization and backscatter measured by WACAL in this campaign is investigated under different conditions. Fig. 2(a)–(d) shows the depolarization-backscatter relationship at an altitude of 0–1, 1–4, 4–7, and 7–12 km, respectively. According to the statistics of the vertical temperature profile during this campaign, the temperature below 1 km altitude was always higher than 0 °C, indicating that there was no ice-phase cloud in this layer [see Fig. 2(a)]. On the contrary, there was no liquid-phase cloud in the layer with a height of 7–12 km [see Fig. 2(d)]. In the altitude range of 1–7 km, liquid, ice and the mixed phase exist simultaneously [see Fig. 2(b) and (c)]. Based on this statistical characteristic, the varying depolarization-backscatter (δ–β) thresholds shown by the gray solid line in Fig. 2 were derived and used in the comprehensive cloud phase classification algorithm.

On this basis, since Z_e is more sensitive to the response of ice crystals, by adding the threshold of this parameter into

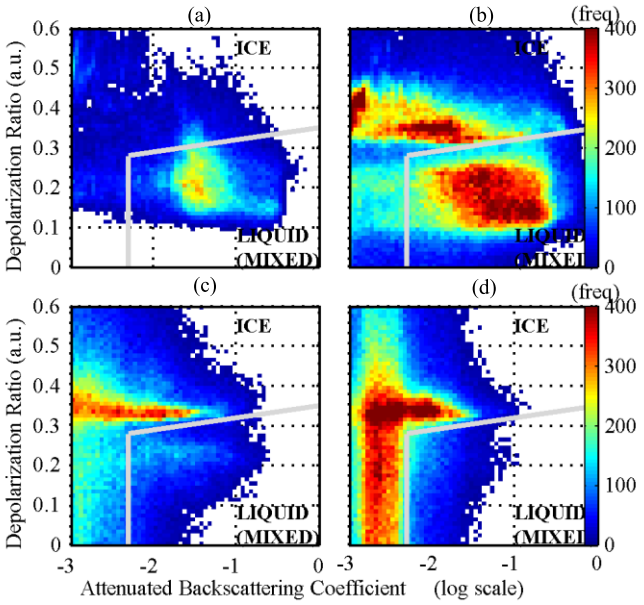

Fig. 2. Frequency of occurrence of clouds as a function of attenuated backscattering coefficient and depolarization ratio for four different height ranges. (a) 0 – 1 km. (b) 1 – 4 km. (c) 4 – 7 km. (d) 7 – 12 km.

TABLE I

CRITERIA FOR CLOUD PHASE CLASSIFICATION ALGORITHM IN THE "LIDAR MEASURED" REGION

Cloud Phase	β (km^{-1} sr^{-1})	δ (a. u.)	Z_e (dBZ)	V_p ($m\ s^{-1}$)
Ice	$>10^{-3}$	above the line	-	-
Liquid	$>10^{-3}$	below the line	<-30	>-1
Mixed-Phase	$>10^{-3}$	below the line	>-30	<-1

the algorithms, the mixed-phase cloud containing both ice and liquid phase that is not identified by lidar products can be identified. V_p is first used to subtract signals from precipitation particles (rain, snow, etc.) due to their significantly faster fall velocities. $V_p < -3$ m s^{-1} is recognized as an indicator of precipitation. Because of the small diameter of liquid cloud droplets, the fall velocity of liquid phase particles is assumed to be approximately zero. To make this classification algorithm clearer and more intuitive, here, the influence of ice particle shapes on the fall velocity has not been considered. The uncertainty introduced by this approach can be reduced by adding additional parameters to the algorithm. Since supercooled water mainly exists in the temperature range of −40 °C to 0 °C, assumptions have been introduced that there is no ice phase above the 0 °C layer and no liquid phase below the −40 °C layer [shadow zone in Fig. 1(a)]. Based on the statistics of various detection parameters in these layers, combined with the previous studies, the thresholds of each parameter in the retrieval algorithm were determined (see Table I). The cloud phase can be classified accordingly based on both WACAL and MMCR measurements. The smaller piece of cloud, which cannot be detected by MMCR, is in the liquid phase, while the larger piece is mainly in the ice phase, except at the cloud top [see Fig. 1(d)].

TABLE II

CRITERIA FOR CLOUD PHASE CLASSIFICATION ALGORITHM OUT OF THE "LIDAR MEASURED" REGION

Cloud Phase	Z_e (dBZ)	V_p ($m\ s^{-1}$)	σ_v ($m\ s^{-1}$)
Ice	<5	-	<0.3
Liquid	<-30	>-1	>0.3
Mixed-Phase	$-30<Z_e<5$	<-1	>0.4

In the zones where cloud existed but WACAL measurement could not reach, MMCR measurement is used to classify the cloud phases. The value of σ_v represents the distributions of velocities within a single radar pixel, which are influenced by the size of hydrometeor, turbulence, and wind shear [see Fig. 1(g)]. When the hydrometeor in the cloud is in a single-phase state, the Doppler spectra tend to show a unimodal distribution. Among them, the Doppler spectra of ice clouds have an especially narrow peak; therefore, when σ_v is large, it means that the hydrometeor in the cloud is not only in a single phase. Combined with the values of Z_e and V_p, the cloud phase in this area can be classified by training with the data from the area identified by both WACAL and MMCR. The thresholds for the classification algorithm are shown in Table II. Then, the cloud phase can be classified in both WACAL-detected and MMCR-detected zones [see Fig. 1(h)]. This algorithm may lead to some uncertainty because MMCR makes it difficult to detect some thin liquid cloud layers. In the region where WACAL measurement cannot reach, the cloud layer classified as the ice phase may still contain some liquid droplets in small quantities. Fig. 1(h) shows the cloud phase classification result of the example by the introduced retrieval algorithm. This retrieval algorithm was only used to classify the cloud phase for nonprecipitating clouds. In situ precipitation measurements from weather stations were used to remove data from precipitating clouds. Fig. 3 shows the flowchart of the cloud phase classification algorithm based on the combined measurement of WACAL and MMCR.

III. RESULTS

A. Phase Classification of Stratiform Clouds

Based on the retrieval algorithm introduced in Section II-B, the cloud phase distribution of several cases with different cloud types was analyzed. It can be seen that during the period shown in Fig. 4, the cloud generally had a stratiform structure over the observation station. The cloud-base height was around 2–3 km, while cloud geometrical thickness was basically kept at around 1–3 km. Fig. 4(a) shows that the atmospheric temperature at the height of 1–6 km was in the range of −40 °C to 0 °C, and the relative humidity at the height where clouds appeared was above 90%. Both WACAL and MMCR captured the echo signals of the clouds completely from midnight to 3:30. During this period, the thickness of the cloud increased with time, while the cloud base height did not change. After 3:30, the signal from ice crystals increased significantly in clouds around 3 km. This caused the attenuation of the lidar signal at this altitude so that it could not pass through the entire cloud layer. An obviously

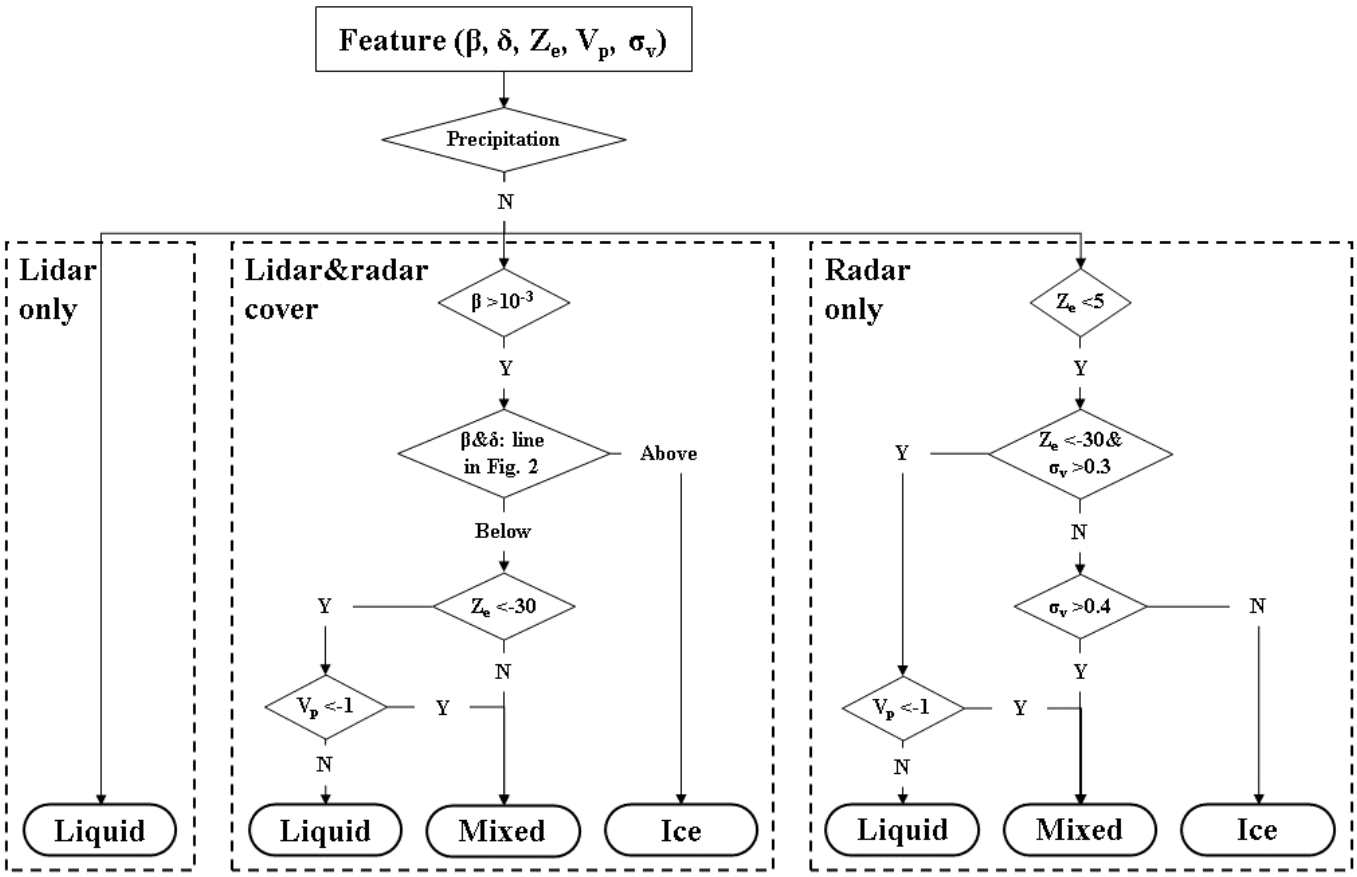

Fig. 3. Flowchart of the cloud phase classification algorithm.

narrow layer of supercooled water was existing at the top of this stratiform cloud. The existence of this layer may be due to the imbalance between the condensate supply rate and the bulk ice crystal mass growth rate [48]. It should be noted that when this supercooled water layer appeared, the cloud top heights detected by MMCR were 100–200 m lower than WACAL, which means that MMCR cannot detect this thin layer. It is reasonable that MMCR has a weak sensitivity to thin liquid clouds. From 3:30 to 5:30, this layer cannot be detected because the lidar signal has been attenuated so much that it cannot reach the "real" cloud top. The cloud top detected by WACAL during this time period (3:30–5:30) cannot be classified as liquid phase due to the higher depolarization ratio there.

B. Phase Classification of Shallow Cumulus Clouds

Typical shallow cumulus clouds were observed by both WACAL and MMCR from 16:00 to 21:00, July 17th (see Fig. 5). Shallow cumulus clouds are characterized by small size, relatively weak convection, and no precipitation, which are dramatically different from those of deep convective clouds (case in Section III-C) [49]. These shallow cumulus clouds were formatted in the afternoon and kept developing during the observed period in Fig. 5. The cloud base was kept stable under 2 km while the cloud top was increased from under 3 km to above 5 km. After 19:00, this cloud system can be regarded as deep cumulus clouds after rapid growth. Through the phase identification of this cloud system, it can be seen that there was also a supercooled water layer on the top of the cumulus clouds, which is similar to the observation results of stratiform clouds introduced in Section III-A. The main body of the cumulus cloud was dominated by liquid phase and mixed phase. As the cloud system developed from shallow cumulus to deep cumulus, the proportion of ice phase in the cloud increased significantly. In the layer from −40 °C to 0 °C, the proportion of the ice phase did not increase with the decrease in temperature. In this case, a potential reason for the rapid cumulus growth is the water vapor transportation from the subcloud mixed layer into the clouds [50]. Because of the signal attenuation, the signal-to-noise ratio of WACAL to the gradually developed cloud was low, while MMCR did not capture the liquid-phase cloud signal below 2 km from 19:00 to 21:00.

C. Phase Classification of Deep Convective Clouds

Deep convective clouds produce a significant proportion of precipitation. These clouds were observed from 16:00 to 19:30 on July 30th (see Fig. 6). Fig. 6(b) shows that the lidar signal was weakened significantly in the deep convective clouds. It could just provide the information of the cloud base, while the radar signal could detect the whole cloud from base to top. The cloud top and cloud base were about 8–11 and

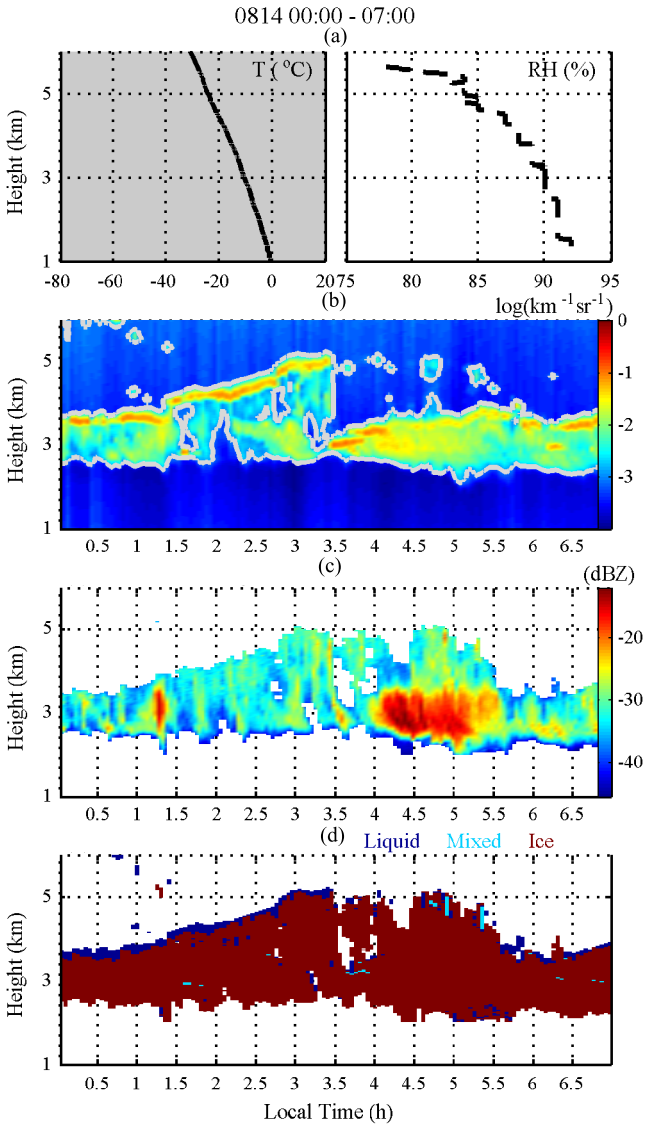

Fig. 4. Characteristics of several parameters in the observation period of 00:00–07:00, August 14th, 2014. (a) Profiles of temperature and relative humidity from the radiosonde, which has the nearest time with remote sensing measurement. (b) Attenuated backscattering coefficients retrieved from WACAL measurements (gray line shows the estimated cloud boundary). (c) Radar reflectivity retrieved from MMCR measurements. (d) Cloud phase classification results (liquid phase: blue; mixed phase: cyan; and ice phase: brown).

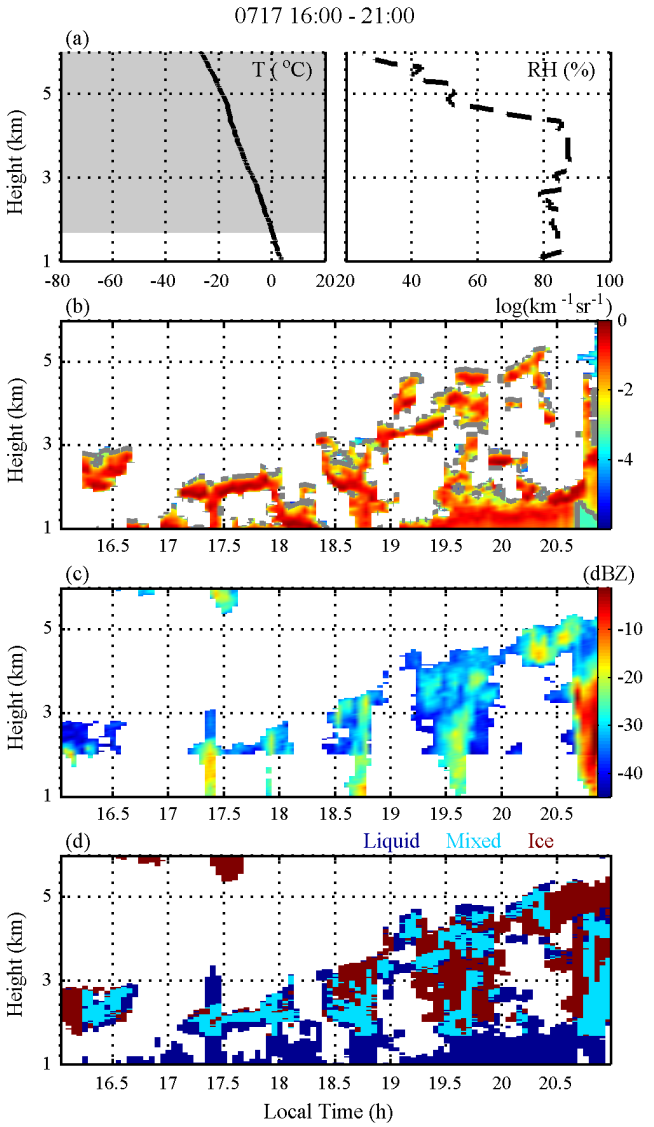

Fig. 5. Characteristics of several parameters in the observation period of 16:00–21:00, July 17th, 2014. (a) Profiles of temperature and relative humidity from the radiosonde, which has the nearest time with remote sensing measurement. (b) Attenuated backscattering coefficients retrieved from WACAL measurements (gray line shows the estimated cloud boundary). (c) Radar reflectivity retrieved from MMCR measurements. (d) Cloud phase classification results (liquid phase: blue; mixed phase: cyan; and ice phase: brown).

1–2 km above the ground, respectively. The liquid droplets were present in the region of the cloud base close to the layer with 0 °C temperature. The mixed-phase regions existed in the layer of 2–8 km in the cloud. Especially from 17:30 to 19:30, there was a mixed-phase layer around 5–6 km height, and this height was also the height where the lidar signal attenuated to zero. Besides, most of the cloud body, in this case, was in the ice phase.

D. Phase Classification of Multilayer Clouds

Except for the phase classification of single-layer clouds, the multilayer clouds are also important targets to be observed. Fig. 7 shows the multilayer clouds observed by WACAL and MMCR at 10:00–13:00 on August 14th. It can be seen from Fig. 7(b) and (c) that it was difficult for WACAL to effectively detect the upper cloud when detecting a multilayer cloud, while MMCR observation would lose the liquid part at the cloud edge of the lower cloud. Generally, the lower cloud was dominated by a liquid phase below 2 km, and the cloud body of 2–5 km had a structure with an internal ice phase and external mixed phase. There was a liquid-phase layer detected at the top of the lower cloud, which shows similar properties to the stratiform cloud. The upper cloud was in the ice phase. In this case, the cloud system was kept at a stable height from 10:00 to 13:00 without obvious development or dissipation.

E. Statistical Characteristics of Cloud Phase in the TIPEX-III

In the TIPEX-III campaign, data within 39 days was obtained. Among them, MMCR ran all day, and WACAL

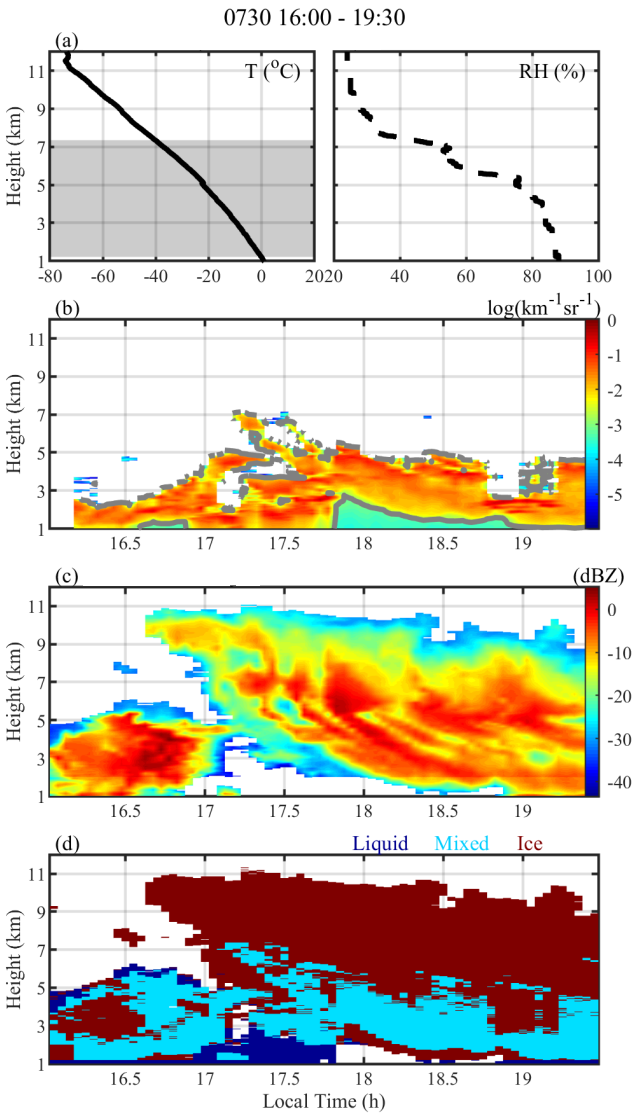

Fig. 6. Characteristics of several parameters in the observation period of 16:00–19:30, July 30th, 2014. (a) Profiles of temperature and relative humidity from the radiosonde, which has the nearest time with remote sensing measurement. (b) Attenuated backscattering coefficients retrieved from WACAL measurements (gray line shows the estimated cloud boundary). (c) Radar reflectivity retrieved from MMCR measurements. (d) Cloud phase classification results (liquid phase: blue; mixed phase: cyan; and ice phase: brown).

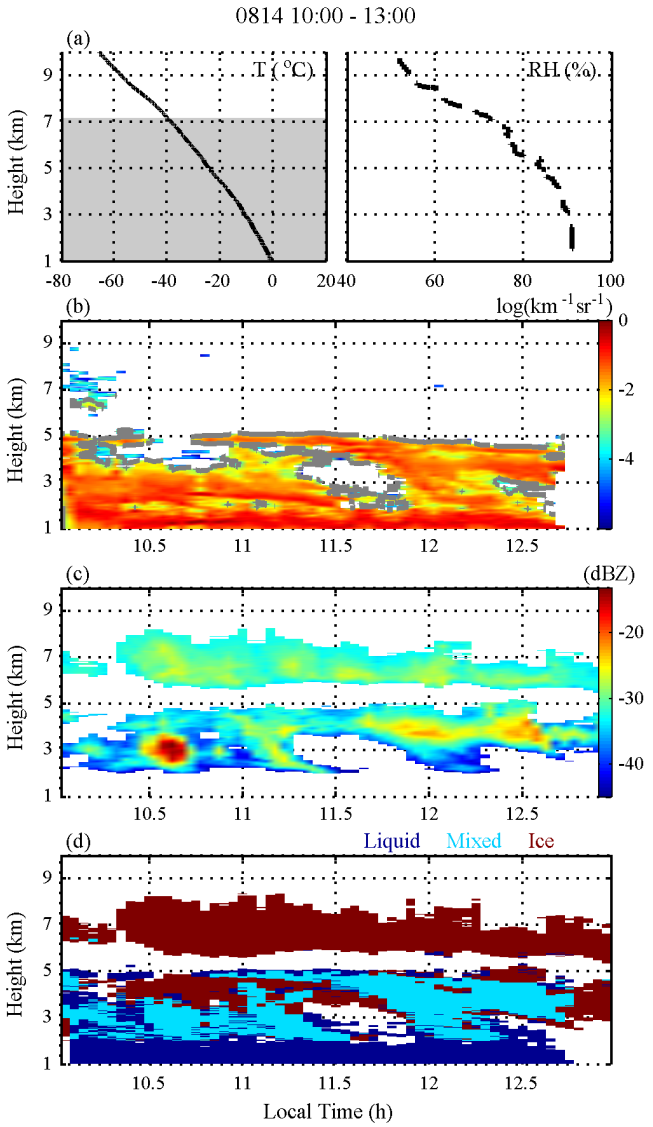

Fig. 7. Characteristics of several parameters in the observation period of 10:00–13:00, August 14th, 2014. (a) Profiles of temperature and relative humidity from the radiosonde, which has the nearest time with remote sensing measurement. (b) Attenuated backscattering coefficients retrieved from WACAL measurements (gray line shows the estimated cloud boundary). (c) Radar reflectivity retrieved from MMCR measurements. (d) Cloud phase classification results (liquid phase: blue; mixed phase: cyan; and ice phase: brown).

mainly ran between 10:00 and 24:00. The MMCR operated alternately in three detection modes with different blind zones, among which the highest blind zone was 2 km. Considering that different amounts of data at different heights would cause deviations in the analyzing results, here, only cloud detections of above 2 km height were selected for statistical analysis.

Fig. 8 shows the diurnal variations of cloud frequencies at different heights during the TIPEX-III campaign. It represents that the frequency of cloud occurrence in Nagqu in summer is obviously high. In particular, the occurrence frequency of low cloud is very high, which is about 50% throughout the day. One obvious reason for the higher low cloud frequency at Nagqu is large-scale convergence and orographic uplift. This finding is consistent with the research results of Wang et al. [50] based on satellite products on the low cloud cover on the TP in summer. Clouds with larger vertical scales also occurred with high frequency, especially in the afternoon. This trend may be related to the elevated land surface with strong radiative heating [51]. Liquid-phase clouds mainly appeared below 4 km height, and the base heights of these clouds were usually below 2 km. The cloud frequencies of liquid and mixed clouds were relatively high in the morning and afternoon. Among them, the cloud frequency of liquid clouds could be up to 0.2 or more during this period and between 0.1 and 0.2 during other periods. Since these low clouds are typically cumulus, this result agrees with the statistical results of Li and Zhang [52] on the frequency of cumulus clouds over the TP in summer based on satellite

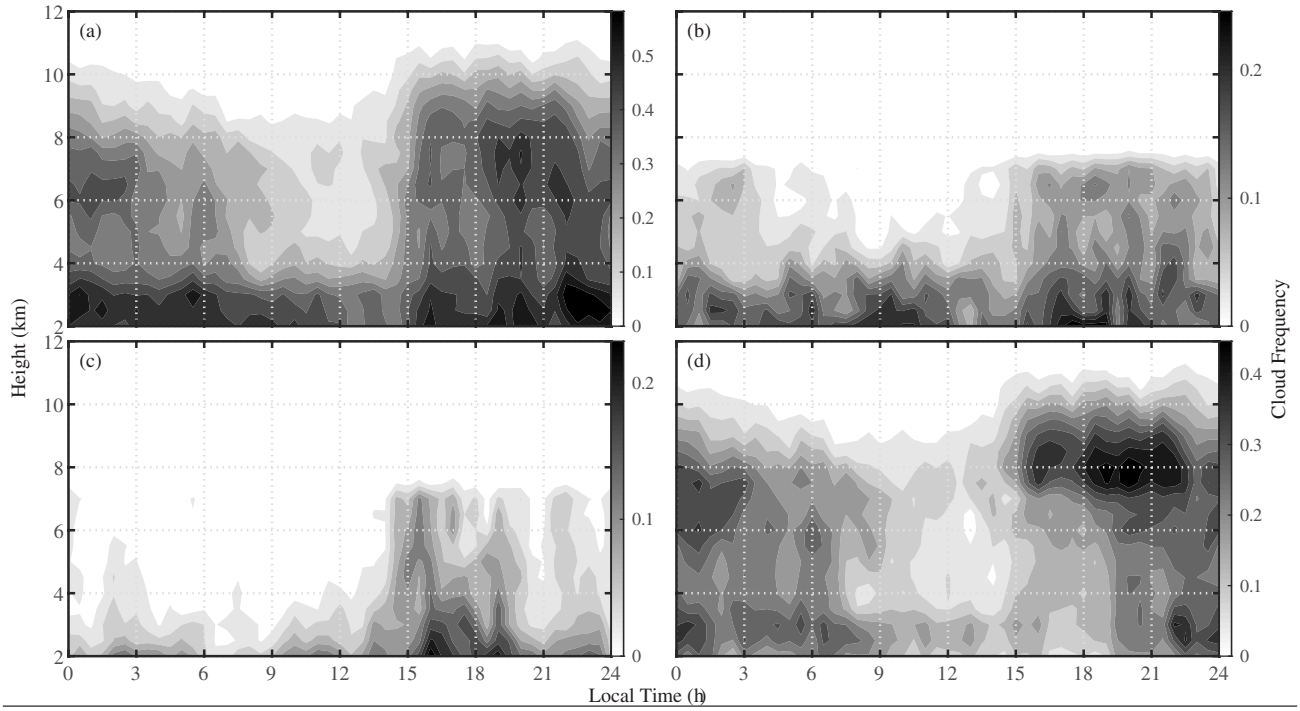

Fig. 8. Diurnal variations of cloud frequencies at different heights during the TIPEX-III campaign. The cloud frequencies of (a) total clouds, (b) liquid phase clouds, (c) mixed-phase clouds, and (d) ice phase clouds are shown, respectively.

data transmitted in the early morning and afternoon. Ice-phase clouds mainly occurred from the afternoon to early morning, with a peak height of 6–8 km. Some of these ice clouds belonged to the upper parts of deep convective clouds developed from shallow cumulus clouds in the afternoon (case in Section III-B). Others belonged to cirrus clouds. This diurnal variation of high-altitude ice clouds shows a similar pattern to ice water content variations investigated by Zhao et al. [13] in the same period in Nagqu.

Fig. 9 shows the frequency distribution of clouds and cloud tops with different phases observed at different heights during the field campaign. It can be seen that liquid, mixed, and ice cloud frequencies were about 0.18, 0.12, and 0.18 at 2 km height above the ground, respectively. Liquid and ice water distributions show an inverse relationship in the atmospheric layer from 2 to 8 km height, where water can exist as a liquid, ice, or a combination of the two. The maximum value of ice cloud frequency, which is approximately 0.3, appeared at 8 km height. The changes in cloud top percentages with altitude show similar patterns [see Fig. 9(b)]. Within the mixed-phase temperature regime (2–8 km), the proportion of liquid phase in the cloud top is significantly higher than that in the cloud body. In the range of 2–5.5 km height, the proportion of liquid phase in cloud top phase is greater than 50%. This phenomenon shows that under similar meteorological conditions (temperature, pressure, et al.), the probability of supercooled water at the top of the cloud is higher than that in the cloud. The existence of this supercooled water may be caused by the imbalance between the condensate supply rate and the bulk ice crystal mass growth rate.

Meanwhile, Fig. 9(b) represents the average temperature profiles measured by radiosonde measurements during this campaign. It can be found that the fractional probabilities

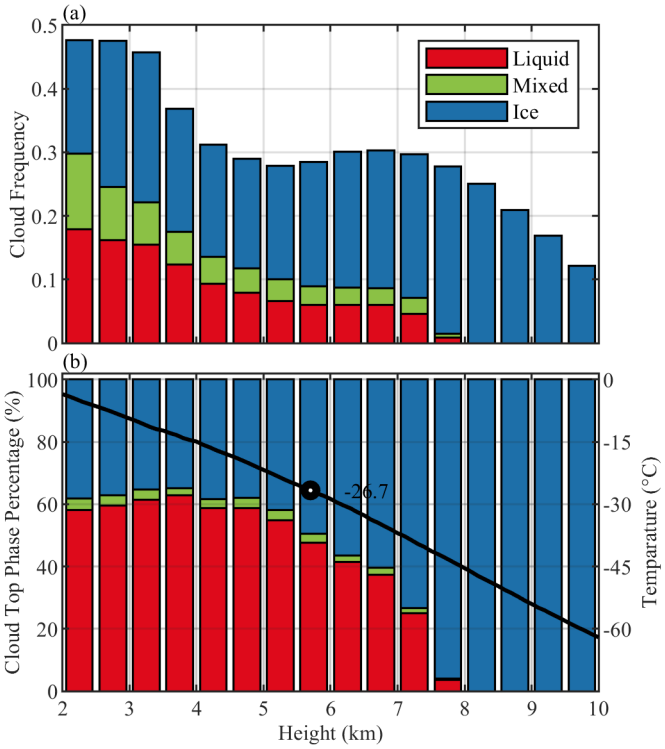

Fig. 9. Occurrence frequency distribution of (a) clouds and (b) cloud tops with different phases observed at different heights during the TIPEX-III campaign (liquid: red; mixed: green; and ice: blue).

of the ice phase and liquid phase in the total cloud top phase intersect at about 5.5–6 km with an average temperature of −26.7 °C. Campbell et al. [53] analyzed the relationship between temperature and cloud top phase with global CALIOP data. This intersection point is −27 °C in their study, which is

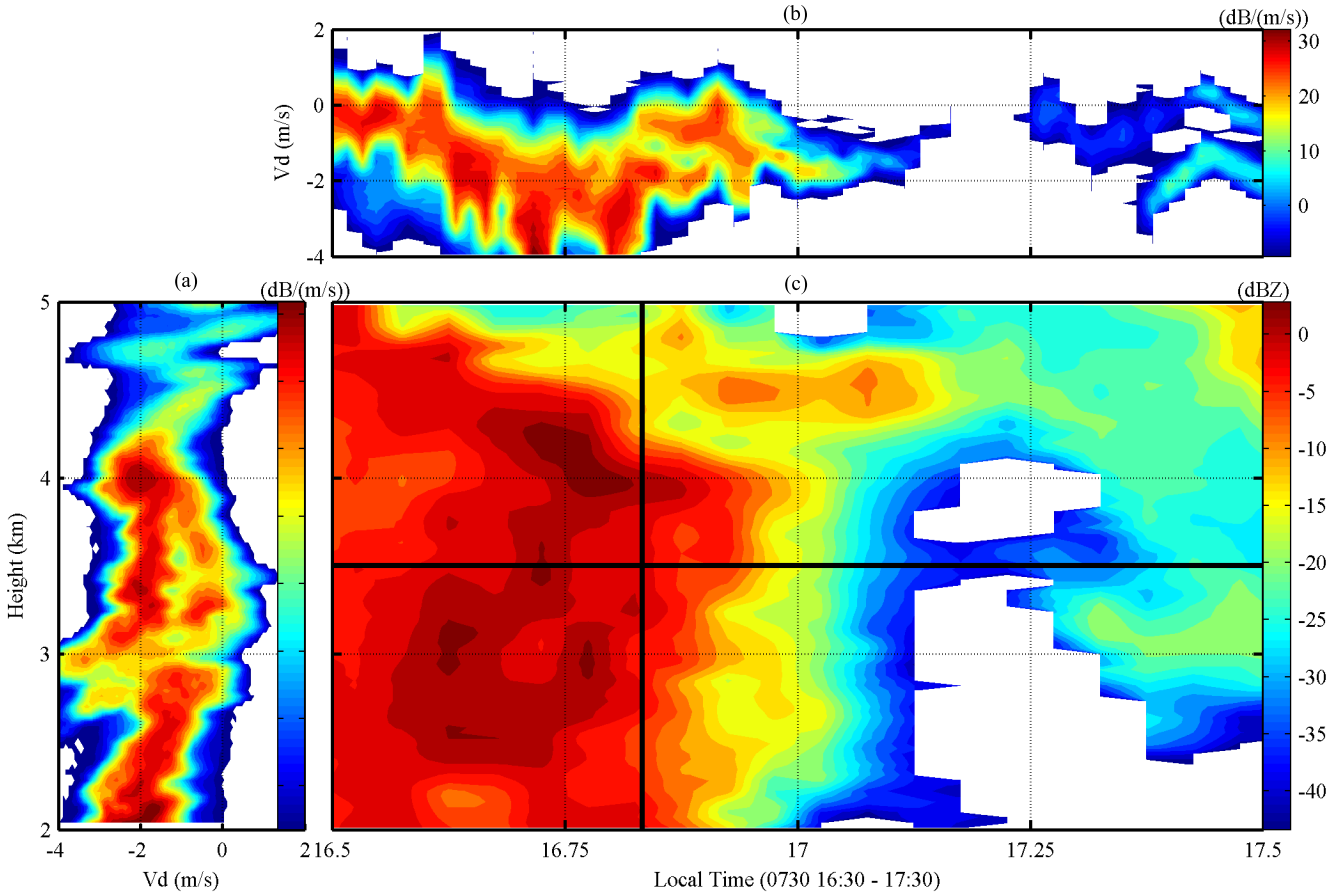

Fig. 10. Raw Doppler spectra data measured by MMCR. (a) Vertical spectrogram at 16:50, July 30th, 2014, along the vertical black line in (c). (b) Time spectrogram at 3.5 km along the horizontal black line in (c). (c) Reflectivity (Z_e) field.

close to the point found in this work. The relationship between the frequency fraction of ice-containing clouds (ice and mixed-phase cloud) in total clouds and the averaged temperature profile is also similar to results from previous studies about heterogeneous ice formations in middle latitudes [54], [55].

IV. Conclusion and Discussions

To better identify and classify the cloud phase, a cloud phase classification algorithm is developed in this study based on the cooperative measurement of lidar and cloud radar. The cloud phase in 2014 at Nagqu over the central TP is classified into three categories, ice, liquid, and mixed phase, by this algorithm based on the field campaign established with a WACAL and a Ka-band MMCR. The cloud phase of different cloud types classified by this algorithm is analyzed. The statistical analysis of the cloud phase classification in the TIPEX-III campaign is investigated and compared with results in other studies.

The cloud phase classification was based on WACAL and MMCR measurements in the TIPEX-III campaign (Nagqu, Tibetan; July–August 2014). Four cases that represent different cloud types were analyzed: stratiform cloud, shallow cumulus cloud, deep convective cloud, and multilayer cloud. Among them, there was an obvious supercooled water layer at the top of the stratiform cloud, while the main parts of cloud bodies remained in the ice phase. This structure was also reported by previous studies about cloud phase measurements all over the world. A case of retrieved shallow cumulus cloud also had this layer at the top, while the main body of this cloud was composed of liquid, mixed, and ice phases. A deep convective cloud retrieved in Section III-C was mainly built by the ice phase, and there were liquid-phase and mixed-phase particles in the middle-lower part of this cloud. For the multilayer cloud case, the upper cloud was mainly in the ice phase, and the lower cloud was similar to the stratiform cloud, which had a supercooled water layer at its top and ice phase particles in the rest part of the cloud body. There is a liquid phase layer that is difficult to be detected by MMCR below 2 km. These case studies show that the WACAL signal could not pass through the thick clouds, while MMCR always missed the cloud droplets at the cloud edge. The retrieval algorithm based on the combination of these instruments can better detect the entire cloud layers.

Based on the data from the TIPEX-III campaign, the diurnal and vertical variations of cloud phase distributions were analyzed. It is obvious that cloud frequency was high at Nagqu in summer, especially the frequency of low cloud, which was around 50% throughout the day. The occurrence frequency of clouds with a larger vertical scale was higher in the afternoon. Liquid-phase clouds always appeared below 4 km height, and the cloud base height was below 2 km typically. The cloud frequencies of liquid and mixed-phase

clouds were relatively higher in the morning and afternoon. Ice clouds mainly occurred from the afternoon to the next morning with a peak height of 6–8 km. Liquid and ice water distributions show an inverse relationship in the atmospheric layer from 2 to 8 km height, where water can exist as a liquid, ice, or a combination of the two. The maximum value of ice cloud frequency, which is approximately 0.3, appeared at 8 km height. The proportion of liquid phase to the cloud top was obviously higher than the proportion to the entire cloud. This phenomenon indicates that the probability of supercooled water at the cloud top is higher than that in the cloud under similar conditions. The fractional probabilities of the ice phase and liquid phase in the total cloud top phase intersect at about −26.7 °C. These statistical analyses provide useful information for further studies about the microphysical characteristics of different cloud phases in the TP.

In future research, the classification algorithm developed in this study has the potential to be continuously modified and optimized. Further parameters can be retrieved from WACAL and MMCR measurements and then added to the algorithm. WACAL-based detection of multiwavelength Raman scattering enables the retrieval of lidar ratio and color ratio indicative the size and types of particles. These parameters can help in distinguishing aerosols, cloud droplets, and horizontally oriented ice crystals [56]. The Doppler spectra measured by MMCR include information about the cloud phase [57]. Fig. 10 shows the raw Doppler spectra data for the deep convective clouds introduced in Section III-C. There was an obvious bimodal distribution of Doppler spectra at the layer with an altitude of 2.5–4 km from 16:45 to 17:30 [see Fig. 10(a) and (b)]. This distribution indicates the presence of mixed-phase clouds. The subjective interpretation of radar Doppler spectra can be effective but inefficient for large datasets; therefore, several statistical descriptors of Doppler spectra that can be used in an automated algorithm are needed [30]. In addition to the Doppler spectrum width used in this study, other descriptors such as left/right slope or Gaussian fitting parameters (one mode or two modes) are also worth adding to the algorithm after processing.

The current cloud phase classification algorithm in this study is specifically designed for nonprecipitating clouds. Based on these expanded retrieval parameters, the classification algorithm can be extended to research related to precipitating clouds and further used to distinguish different types of precipitation particles, such as rain, snow, graupel, and hail.

ACKNOWLEDGMENT

The authors would like to thank the researchers who joined the Third Tibetan Plateau Atmospheric Scientific Experiment (TIPEX-III) campaign for their kind help.

REFERENCES

[1] J. H. Seinfeld and S. N. Pandis, *Atmospheric Chemistry and Physics*. 2nd ed. Hoboken, NJ, USA: Wiley, 2006.

[2] J. Straka, *Cloud Precipitation Microphysics*. Cambridge, U.K.: Cambridge Univ. Press, 2009.

[3] R. K. Pachauri et al., *Climate Change 2014: Synthesis Report. Contribution of Working Groups I, II and III to the Fifth Assessment Report of the Intergovernmental Panel on Climate Change*. Geneva, Switzerland: IPCC, 2014, p. 151.

[4] Y. Wang et al., "Diverse dispersion effects and parameterization of relative dispersion in urban fog in eastern China," *J. Geophys. Res., Atmos.*, vol. 128, no. 6, Mar. 2023, Art. no. e2022JD037514, doi: 10.1029/2022JD037514.

[5] R. J. Hogan, M. D. Behera, E. J. O'Connor, and A. J. Illingworth, "Estimate of the global distribution of stratiform supercooled liquid water clouds using the LITE LiDAR," *Geophys. Res. Lett.*, vol. 31, no. 5, Mar. 2004, Art. no. L05106, doi: 10.1029/2003GL018977.

[6] Z. Sun and K. P. Shine, "Studies of the radiative properties of ice and mixed-phase clouds," *Quart. J. Roy. Meteorol. Soc.*, vol. 120, no. 515, pp. 111–137, Jan. 1994, doi: 10.1002/qj.49712051508.

[7] X. Xu et al., "Effects of cloud liquid-phase microphysical processes in mixed-phase cumuli over the Tibetan Plateau," *J. Geophys. Res., Atmos.*, vol. 125, no. 19, Oct. 2020, Art. no. e2020JD033371, doi: 10.1029/2020JD033371.

[8] R. M. Forbes and M. Ahlgrimm, "On the representation of high-latitude boundary layer mixed-phase cloud in the ECMWF global model," *Monthly Weather Rev.*, vol. 142, no. 9, pp. 3425–3445, Sep. 2014, doi: 10.1175/mwr-d-13-00325.1.

[9] W. Gao, L. Liu, J. Li, and C. Lu, "The microphysical properties of convective precipitation over the Tibetan Plateau by a subkilometer resolution cloud-resolving simulation," *J. Geophys. Res., Atmos.*, vol. 123, no. 6, pp. 3212–3227, Mar. 2018, doi: 10.1002/2017jd027812.

[10] P. Zhao et al., "The third atmospheric scientific experiment for understanding the Earth–atmosphere coupled system over the Tibetan Plateau and its effects," *Bull. Amer. Meteorol. Soc.*, vol. 99, no. 4, pp. 757–776, Apr. 2018, doi: 10.1175/bams-d-16-0050.1.

[11] W. R. Boos and Z. Kuang, "Dominant control of the South Asian monsoon by orographic insulation versus Plateau heating," *Nature*, vol. 463, no. 7278, pp. 218–222, Jan. 2010, doi: 10.1038/nature08707.

[12] S. Luo et al., "Parameterizations of entrainment-mixing mechanisms and their effects on cloud droplet spectral width based on numerical simulations," *J. Geophys. Res., Atmos.*, vol. 125, no. 22, Nov. 2020, Art. no. e2020JD032972, doi: 10.1029/2020JD032972.

[13] C. Zhao et al., "Toward understanding the properties of high ice clouds at the Naqu site on the Tibetan Plateau using ground-based active remote sensing measurements obtained during a short period in July 2014," *J. Appl. Meteorol. Climatol.*, vol. 55, no. 11, pp. 2493–2507, Nov. 2016, doi: 10.1175/jamc-d-16-0038.1.

[14] I. Tan, T. Storelvmo, and M. D. Zelinka, "Observational constraints on mixed-phase clouds imply higher climate sensitivity," *Science*, vol. 352, no. 6282, pp. 224–227, Apr. 2016, doi: 10.1126/science.aad5300.

[15] S. J. Moss and D. W. Johnson, "Aircraft measurements to validate and improve numerical model parametrisations of ice to water ratios in clouds," *Atmos. Res.*, vol. 34, nos. 1–4, pp. 1–25, Jun. 1994, doi: https://doi.org/10.1016/0169-8095(94)90078-7.

[16] A. V. Korolev, G. A. Isaac, S. G. Cober, J. W. Strapp, and J. Hallett, "Microphysical characterization of mixed-phase clouds," *Quart. J. Roy. Meteorol. Soc.*, vol. 129, no. 587, pp. 39–65, Jan. 2003, doi: 10.1256/qj.01.204.

[17] R. J. Hogan, P. N. Francis, H. Flentje, A. J. Illingworth, M. Quante, and J. Pelon, "Characteristics of mixed-phase clouds. I: LiDAR, radar and aircraft observations from CLARE'98," *Quart. J. Roy. Meteorol. Soc.*, vol. 129, no. 592, pp. 2089–2116, Jul. 2003, doi: 10.1256/rj.01.208.

[18] S. M. Sekelsky and R. E. McIntosh, "Cloud observations with a polarimetric 33 GHz and 95 GHz radar," *Meteorol. Atmos. Phys.*, vol. 59, nos. 1–2, pp. 123–140, 1996, doi: 10.1007/bf01032004.

[19] Z. Wang and K. Sassen, "Cirrus cloud microphysical property retrieval using LiDAR and radar measurements. Part II: Midlatitude cirrus microphysical and radiative properties," *J. Atmos. Sci.*, vol. 59, no. 14, pp. 2291–2302, Jul. 2002, doi: 10.1175/1520-0469(2002)059<2291:CCMPRU>2.0.CO;2.

[20] C. Zhao and T. J. Garrett, "Ground-based remote sensing of precipitation in the Arctic," *J. Geophys. Res.*, vol. 113, no. D14, 2008, Art. no. D14204, doi: 10.1029/2007JD009222.

[21] K. P. Moran, B. E. Martner, M. J. Post, R. A. Kropfli, D. C. Welsh, and K. B. Widener, "An unattended cloud-profiling radar for use in climate research," *Bull. Amer. Meteorol. Soc.*, vol. 79, no. 3, pp. 443–456, Mar. 1998, doi: 10.1175/1520-0477(1998)079<0443:AUCPRF>2.0.CO;2.

[22] M. D. Shupe, P. Kollias, S. Y. Matrosov, and T. L. Schneider, "Deriving mixed-phase cloud properties from Doppler radar spectra," *J. Atmos. Ocean. Technol.*, vol. 21, no. 4, pp. 660–670, Apr. 2004, doi: 10.1175/1520-0426(2004)021<0660:DMCPFD>2.0.CO;2.

[23] Y. Bian, W. Xu, Y. Hu, J. Tao, Y. Kuang, and C. Zhao, "Method to retrieve aerosol extinction profiles and aerosol scattering phase functions with a modified CCD laser atmospheric detection system," *Opt. Exp.*, vol. 28, no. 5, pp. 6631–6647, 2020, doi: 10.1364/oe.386214.

[24] C. Weitkamp, *LiDAR: Range-Resolved Optical Remote Sensing of the Atmosphere*. New York, NY, USA: Springer, 2005.

[25] Y. Bian et al., "A novel method to retrieve the nocturnal boundary layer structure based on CCD laser aerosol detection system measurements," *Remote Sens. Environ.*, vol. 211, pp. 38–47, Jun. 2018, doi: 10.1016/j.rse.2018.04.007.

[26] C. Zhao, Y. Wang, Q. Wang, Z. Li, Z. Wang, and D. Liu, "A new cloud and aerosol layer detection method based on micropulse LiDAR measurements," *J. Geophys. Res., Atmos.*, vol. 119, no. 11, pp. 6788–6802, Jun. 2014, doi: 10.1002/2014JD021760.

[27] K. Sassen, "The polarization LiDAR technique for cloud research: A review and current assessment," *Bull. Amer. Meteorol. Soc.*, vol. 72, no. 12, pp. 1848–1866, Dec. 1991, doi: 10.1175/1520-0477(1991)072<1848:TPLTFC>2.0.CO;2.

[28] V. Noel, "Classification of particle shapes from LiDAR depolarization ratio in convective ice clouds compared to in situ observations during CRYSTAL-FACE," *J. Geophys. Res.*, vol. 109, no. D24, 2004, Art. no. D24213, doi: 10.1029/2004jd004883.

[29] H. Xie et al., "Automated detection of cloud and aerosol features with SACOL micro-pulse LiDAR in Northwest China," *Opt. Exp.*, vol. 25, no. 24, pp. 30732–30753, Nov. 2017, doi: 10.1364/oe.25.030732.

[30] L. D. Riihimaki, J. M. Comstock, E. Luke, T. J. Thorsen, and Q. Fu, "A case study of microphysical structures and hydrometeor phase in convection using radar Doppler spectra at Darwin, Australia," *Geophys. Res. Lett.*, vol. 44, no. 14, pp. 7519–7527, Jul. 2017, doi: 10.1002/2017gl074187.

[31] H. C. Van de Hulst, *Light Scattering by Small Particles*. New York, NY, USA: Dover, 1957.

[32] T. J. Garrett and C. Zhao, "Ground-based remote sensing of thin clouds in the Arctic," *Atmos. Meas. Techn.*, vol. 6, no. 5, pp. 1227–1243, May 2013, doi: 10.5194/amt-6-1227-2013.

[33] Z. Wang and K. Sassen, "Cirrus cloud microphysical property retrieval using LiDAR and radar measurements. Part I: Algorithm description and comparison with in situ data," *J. Appl. Meteorol.*, vol. 41, no. 3, pp. 218–229, 2002, doi: 10.1175/1520-0450(2002)041<0218:CCMPRU>2.0.CO;2.

[34] S. Khanal and Z. Wang, "Evaluation of the LiDAR–radar cloud ice water content retrievals using collocated in situ measurements," *J. Appl. Meteorol. Climatol.*, vol. 54, no. 10, pp. 2087–2097, Oct. 2015, doi: 10.1175/jamc-d-15-0040.1.

[35] M. D. Shupe, S. Y. Matrosov, and T. Uttal, "Arctic mixed-phase cloud properties derived from surface-based sensors at SHEBA," *J. Atmos. Sci.*, vol. 63, no. 2, pp. 697–711, Feb. 2006, doi: 10.1175/jas3659.1.

[36] C. Zhao et al., "Toward understanding of differences in current cloud retrievals of ARM ground-based measurements," *J. Geophys. Res., Atmos.*, vol. 117, no. D10, May 2012, Art. no. D10206, doi: 10.1029/2011jd016792.

[37] E. P. Luke, P. Kollias, and M. D. Shupe, "Detection of supercooled liquid in mixed-phase clouds using radar Doppler spectra," *J. Geophys. Res.*, vol. 115, no. D19, 2010, Art. no. D19201, doi: 10.1029/2009jd012884.

[38] J. Yin et al., "East Asia reanalysis system (EARS)," *Earth Syst. Sci. Data*, vol. 15, no. 6, pp. 2329–2346, Jun. 2023, doi: 10.5194/essd-15-2329-2023.

[39] L. Liu et al., "Comprehensive radar observations of clouds and precipitation over the Tibetan Plateau and preliminary analysis of cloud properties," *J. Meteorol. Res.*, vol. 29, no. 4, pp. 546–561, Aug. 2015, doi: 10.1007/s13351-015-4208-6.

[40] Q. S. He et al., "The properties and formation of cirrus clouds over the Tibetan Plateau based on summertime LiDAR measurements," *J. Atmos. Sci.*, vol. 70, no. 3, pp. 901–915, Mar. 2013, doi: 10.1175/jas-d-12-0171.1.

[41] C. Zhao, L. Liu, Q. Wang, Y. Qiu, Y. Wang, and X. Wu, "MMCR-based characteristic properties of non-precipitating cloud liquid droplets at Naqu site over Tibetan Plateau in July 2014," *Atmos. Res.*, vol. 190, pp. 68–76, Jul. 2017, doi: 10.1016/j.atmosres.2017.02.002.

[42] G. Dai, S. Wu, X. Song, and L. Liu, "Optical and geometrical properties of cirrus clouds over the Tibetan Plateau measured by LiDAR and radiosonde sounding during the summertime in 2014," *Remote Sens.*, vol. 11, no. 3, p. 302, Feb. 2019. [Online]. Available: http://www.mdpi.com/2072-4292/11/3/302

[43] S. Wu, G. Dai, X. Song, B. Liu, and L. Liu, "Observations of water vapor mixing ratio profile and flux in the Tibetan Plateau based on the LiDAR technique," *Atmos. Meas. Techn.*, vol. 9, no. 3, pp. 1399–1413, Apr. 2016, doi: 10.5194/amt-9-1399-2016.

[44] J. Zheng, L. Liu, K. Zhu, J. Wu, and B. Wang, "A method for retrieving vertical air velocities in convective clouds over the Tibetan Plateau from TIPEX-III cloud radar Doppler spectra," *Remote Sens.*, vol. 9, no. 9, p. 964, Sep. 2017. [Online]. Available: http://www.mdpi.com/2072-4292/9/9/964

[45] S. R. Pal, W. Steinbrecht, and A. I. Carswell, "Automated method for LiDAR determination of cloud-base height and vertical extent," *Appl. Opt.*, vol. 31, no. 10, pp. 1488–1494, Apr. 1992, doi: 10.1364/ao.31.001488.

[46] S. Wu et al., "Mobile multi-wavelength polarization Raman LiDAR for water vapor, cloud and aerosol measurement," *Opt. Exp.*, vol. 23, no. 26, pp. 33870–33892, Dec. 2015, doi: 10.1364/oe.23.033870.

[47] Y. Hu et al., "CALIPSO/CALIOP cloud phase discrimination algorithm," *J. Atmos. Ocean. Technol.*, vol. 26, no. 11, pp. 2293–2309, Nov. 2009, doi: 10.1175/2009jtecha1280.1.

[48] R. M. Rauber and A. Tokay, "An explanation for the existence of supercooled water at the top of cold clouds," *J. Atmos. Sci.*, vol. 48, no. 8, pp. 1005–1023, Apr. 1991.

[49] H. Shi et al., "Intensive radiosonde measurements of summertime convection over the inner Mongolia grassland in 2014: Difference between shallow cumulus and other conditions," *Adv. Atmos. Sci.*, vol. 34, no. 6, pp. 783–790, Jun. 2017, doi: 10.1007/s00376-017-6284-2.

[50] Y. Wang et al., "Why are there more summer afternoon low clouds over the Tibetan Plateau compared to eastern China?" *Geophys. Res. Lett.*, vol. 47, no. 23, Dec. 2020, Art. no. e2020GL089665, doi: 10.1029/2020GL089665.

[51] S. Sugimoto and K. Ueno, "Role of mesoscale convective systems developed around the eastern Tibetan Plateau in the eastward expansion of an upper tropospheric high during the monsoon season," *J. Meteorol. Soc. Jpn. II*, vol. 90, no. 2, pp. 297–310, 2012, doi: 10.2151/jmsj.2012-209.

[52] Y. Li and M. Zhang, "Cumulus over the Tibetan Plateau in the summer based on CloudSat–CALIPSO data," *J. Climate*, vol. 29, no. 3, pp. 1219–1230, Feb. 2016, doi: 10.1175/JCLI-D-15-0492.1.

[53] J. R. Campbell, M. A. Vaughan, M. Oo, R. E. Holz, J. R. Lewis, and E. J. Welton, "Distinguishing cirrus cloud presence in autonomous LiDAR measurements," *Atmos. Meas. Techn.*, vol. 8, no. 1, pp. 435–449, Jan. 2015, doi: 10.5194/amt-8-435-2015.

[54] J. Bühl, A. Ansmann, P. Seifert, H. Baars, and R. Engelmann, "Toward a quantitative characterization of heterogeneous ice formation with LiDAR/radar: Comparison of CALIPSO/CloudSat with ground-based observations," *Geophys. Res. Lett.*, vol. 40, no. 16, pp. 4404–4408, Aug. 2013, doi: 10.1002/grl.50792.

[55] D. Zhang, Z. Wang, and D. Liu, "A global view of midlevel liquid-layer topped stratiform cloud distribution and phase partition from CALIPSO and CloudSat measurements," *J. Geophys. Res.*, vol. 115, Feb. 2010, Art. no. D00H13, doi: 10.1029/2009JD012143.

[56] H. Okamoto et al., "Interpretation of LiDAR ratio and depolarization ratio of ice clouds using spaceborne high-spectral-resolution polarization LiDAR," *Opt. Exp.*, vol. 27, pp. 36587–36600, Dec. 2019, doi: 10.1364/OE.27.036587.

[57] H. Kalesse, W. Szyrmer, S. Kneifel, P. Kollias, and E. Luke, "Fingerprints of a riming event on cloud radar Doppler spectra: Observations and modeling," *Atmos. Chem. Phys.*, vol. 16, no. 5, pp. 2997–3012, Mar. 2016, doi: 10.5194/acp-16-2997-2016.

Yuxuan Bian received the B.S. degree from the Nanjing University of Information Science and Technology, Nanjing, Jiangsu, China, in 2011, and the Ph.D. degree in atmospheric physics and atmospheric environment from Peking University, Beijing, China, in 2016.

He is currently an Associate Professor with the State Key Laboratory of Severe Weather, Chinese Academy of Meteorological Sciences, Beijing. His research interests include aerosol optical and hygroscopicity properties, cloud microphysical characteristics, and the development of instruments for measuring aerosol/cloud properties.

Liping Liu received the M.S. degree in atmospheric physics from the Lanzhou Institute of Atmospheric Physics, CAS, Lanzhou, Gansu, China, in 1988, and the Ph.D. degree from Nanjing University, Nanjing, Jiangsu, China, in 1997.

In 1989, he joined the Lanzhou Institute of Atmospheric Physics, CAS, as a Researcher for radar meteorology. Since 2020, he has been the Chief Scientist with the Radar Meteorology and Application Research Team, Chinese Academy of Meteorological Sciences, Beijing, China. His research interests include the data quality control and retrieval algorithms for microphysical and dynamic parameters in cloud and precipitation based on dual-polarization weather radar, phased array weather radar, and cloud radar measurement.

Jiafeng Zheng received the Ph.D. degree from the Nanjing University of Information Science and Technology, Nanjing, Jiangsu, China, in 2016.

He is currently an Associate Professor with the School of Atmospheric Sciences, Chengdu University of Information Technology, Chengdu, Sichuan, China. His research is focused on cloud and precipitation sounding by remote sensors.

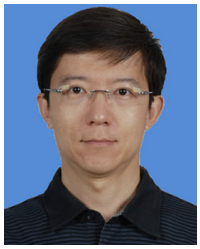

Songhua Wu received the B.S. degree in electronics and information systems and the Ph.D. degree in physical oceanography from the Ocean University of China, Qingdao, Shandong, China, in 1999 and 2004, respectively.

He is currently a Professor with the College of Marine Technology, Faculty of Information Science and Engineering, Ocean University of China. He is also a Visiting Senior Scientist with IPA/DLR, Oberpfaffenhofen, Germany. His research interests include atmospheric and oceanic lidar development and application, signal processing, and laser spectroscopy.

Guangyao Dai received the B.S. degree in physics and the Ph.D. degree in marine detection technology from the Ocean University of China, Qingdao, Shandong, China, in 2012 and 2019, respectively.

He is currently an Associate Professor with the College of Marine Technology, Faculty of Information Science and Engineering, Ocean University of China. His research interests focus on the atmospheric and oceanic lidar development and scientific application of lidar measurements.